IVYSPRING INTERNATIONAL PUBLISHER

Theranostics

2022; 12(9): 4163-4180. doi: 10.7150/thno.71873

Research Paper

# Spatial maps of hepatocellular carcinoma transcriptomes reveal spatial expression patterns in tumor immune microenvironment

Yue-fan Wang[1*], Sheng-xian Yuan[2*], Hui Jiang[3*], Zhi-xuan Li[4*], Hao-zan Yin[1], Jian Tan[1], Zhi-hui Dai[1], Chun-mei Ge[1], Shu-han Sun[1] and Fu Yang[1]✉

1. The department of Medical Genetics, Naval Medical University, Shanghai, 200433, China.
2. The Third Department of Hepatic Surgery, Eastern Hepatobiliary Surgery Hospital Affiliated to Naval Medical University, Shanghai, 200438, China.
3. Department of Pathology, Changhai Hospital Affiliated to Navy Medical University, Shanghai, 200433, China.
4. Translational Medicine Research Center, Medical Innovation Research Division and Fourth Medical Center of the Chinese PLA General Hospital, Beijing, 100048, China.

* Equal contribution

✉ Corresponding author: Fu Yang, E-mail: yangfusq1997@smmu.edu.cn, The Department of Medical Genetics, Naval Medical University, Shanghai, 200433, China.



Received: 2022.02.09; Accepted: 2022.05.06; Published: 2022.05.16

## Abstract

**Rationale:** Hepatocellular carcinoma (HCC) is a highly heterogeneous and malignant disease with the complex immune microenvironment, which ultimately influence clinic outcomes of patients. However, the spatial expression patterns of diverse immune cells among tumor microenvironment remain to be further deciphered.

**Methods:** Spatial transcriptomics sequencing (ST) was implemented on two portions of HCC specimens. Differentially expressed genes, cell cycle phases, epithelial-mesenchymal features, pseudo-time and immune infiltration analysis were applied to demonstrate the intratumor heterogeneity and define the specific immune-related regions, and the results were further validated by a second analysis on another ST study. *In vitro* and *in vivo* experiments were conducted to confirm the functional mechanisms of key molecules such as CCL15, CCL19 and CCL21. Clinical tissue samples were used to assess their potential prognostic and therapeutic values.

**Results:** Totally, 7553 spots were categorized into 15 subsets by hierarchical clustering, and malignant subsets with intratumor heterogeneity phenotypes were identified. Spatial heterogeneity from distinct sectors highlights specific chemokines: CCL15 is remarkable in the core region of the carcinoma sector and facilitates the immunosuppressive microenvironment by recruiting and polarizing M2-like macrophages *in vitro* and *in vivo*; High expression of CCL15 and CD163 respectively predicts poor prognosis of HCC patients, and the combined application of them has better predictive value. CCL19 and CCL21, sharing similar spatial expression patterns, are highly-correlated and prominent in the immune infiltration enrichment and recruit $CD3^+$ T cells and $CD20^+$ B cells to inhibit the growth of HCC, indicating a good prognosis of HCC patients.

**Conclusions:** Taken together, our studies preliminarily reveal intratumor heterogeneity of HCC based on ST techniques and unravel the previously unexplored spatial expression patterns in the immune microenvironment. We also highlight the clinical significance and spatial discrepancy of key molecules, providing novel insight for further developing therapeutic strategies in HCC.

Key words: hepatocellular carcinoma, spatial transcriptomics, heterogeneity, immune microenvironment

## Introduction

The latest cancer statistics for 2020 indicate that primary liver cancer (PLC) ranks sixth in morbidity and third in mortality worldwide, with approximately 906,000 new cases and 830,000 deaths yearly, and that hepatocellular carcinoma (HCC) accounts for approximately 80% of PLC cases [1]. Vaccination

against hepatitis B virus (HBV) and reduction in aflatoxin exposure have sharply decreased the incidence of HCC in recent decades [2]. HCC screening and early diagnosis, as well as advances in surgery and molecular targeted medicine, have dramatically reduced the mortality rate of HCC to a certain extent. Nonetheless, there still exist clinical phenomena in which although the clinicopathological stages of some patients are consistent, major discrepancies due to tumor heterogeneity are noted regarding drug sensitivity and prognosis after operation [3].

Tumor heterogeneity in HCC can be roughly classified into phenotypic heterogeneity and molecular heterogeneity [4], with the former being observed from pathological and morphological perspectives and the latter being documented at three levels: interpatient, intertumoral, and intratumor heterogeneity [5, 6]. Previous studies have attempted to profile the landscape of molecular heterogeneity in HCC [7-9]; nevertheless, due to discrepancies, the roles of various factors in liver carcinogenesis and progression remain ill-defined. Accumulating evidence has found that tumor heterogeneity is closely associated with the immune environment, which is characterized by three immunosubtypes (immune-high, immune-mid, and immune-low) with noteworthily distinct prognoses [10]. Notably, single-cell RNA sequencing (scRNA-seq) has dramatically enriched our knowledge of tumor heterogeneity in tumor cell subpopulations, the immune microenvironment, and the cell developmental trajectory of HCC [11-13]. Whereas spatial information is disrupted after tissue dissection into a single-cell suspension, disengaging gene expression from its original tissue architecture and rendering exploration of the authentic appearance of gene expression patterns difficult [14]. In this scenario, emerging spatial transcriptomics (ST) technology has the attributes of spatially localizing function resulting from gene expression, which can be a perfect complement to scRNA sequencing. ST was first applied in the mouse brain and human breast cancer to verify the feasibility of spatial visualization and quantitative analysis of gene expression [15]; it was then used to explore the spatial discrepancy of gene expression in dynamic disease processes, such as amyotrophic lateral sclerosis [16] and Alzheimer's disease [17], as well as in normal tissue development processes [18]. Moreover, ST is conducive to resolving spatial heterogeneity and spatial gene expression patterns in various tumors, such as prostate cancer [19], melanoma [20] and pancreatic ductal adenocarcinoma [21], and primary liver cancer [22, 23].

In the present study, we performed ST sequencing for two portions of HCC specimens with clearly demarcated and continuous cores, peripheral regions, and boundary regions and investigated the potential makers and regulatory mechanisms of immunosuppressive or immune enrichment regions with distinct prognoses based on analyzing spatial gene expression patterns. Accordingly, our studies highlighted the spatial heterogeneity of gene expression patterns as well as their clinical significance in the tumor immune microenvironment and provided novel insight for the further prognostic and therapeutic strategies for HCC.

## Materials and Methods

### Specimens and clinical data

Totally, two fresh continuous tissues (from tumor tissue, tumor boundary region to para-tumor tissue) of one HCC case were acquired from surgical resections without preoperative treatment at Eastern Hepatobiliary Surgery Hospital (EHBH, Shanghai, China). Another 89 HCC tissues were obtained from the Department of Pathology at Changhai Hospital (CH, Shanghai, China). Diagnoses of HCC were evaluated by two certificated pathologists. Collections of tissue specimens were approved by the Ethics Committee of EHBH and CH, respectively. Written informed consent was provided by individuals donating HCC tissues. Fresh tissues for ST sequencing were promptly filled with optimal cutting temperature (OCT) compound and then snap frozen in isopentane and liquid nitrogen. The samples used for Western blotting were freshly frozen in -80 °C until use. Tissues utilized for immunohistochemistry analysis were formalin fixed and paraffin embedded (FFPE). Clinical characteristics from CH cohort were listed in Table S1.

### Spatial transcriptomics sequencing and bioinformatic analysis

#### Spatial transcriptomics sequencing

The two fresh HCC tissues were surgically resected, washed with pre-cooled PBS solution and drained by gauzes. The tissues were then transferred to isopentane for soaking and freezing, and moved to a cryopreservation tube with tweezers for subsequent embedding with the OCT mixture. The procedures are as follows: (1) Hematoxylin-eosin staining (HE) was used for histological imaging; (2) Tissues were then fixed, stained and permeabilized to release mRNA, which can bind to the probes that contained a 16 bp spot barcode and a 12 bp UMI sequence. The capturing probe with poly (dT) sequence acquired gene expression information by binding to mRNA

3'-poly(A) tail; (3) cDNA synthesis and sequencing libraries were prepared using the captured RNA as templates; (4) This sequencing was based on 10× Genomics Visium and the paired-end sequencing mode of the Illumina sequencing platform, which was previously described before [24].

### Data processing and quality control

After sequencing, the data were visualized and analyzed via Space Ranger (version1.1.0). The Space Ranger was used to ensemble the reference genome database and FastQC software was utilized for data quality control. Further sequencing and application of R software and other applications were used for data visualization.

R software version 4.0.3 and "Seurat" software package version 3.1.1 were used for analysis. After excluding low-quality units, we used the "SCTransform" function to normalize data, find variable features and scale data.

### Dimensionality reduction analysis

Next, principal component analysis (PCA) was performed on the first 2000 highly variable genes using the "RunPCA" function. Then, the number of PCs corresponding to ElbowPlot was selected and the "RunUMAP" function with a default perplexity value of 30 was executed to obtain the bidimensional coordinates for single-spot. At the same time, we used the "FindClusters" function to cluster the unsupervised units at 0.6 resolution on the same PC as for the "RunUMAP" function. Therefore, the datasets were visualized through UMAP plots. The closer the spot distance was, the closer the expression trend of spot was.

### Differentially expressed gene analysis

The "FinAllMarkers" function is used to identify the differentially expressed genes (DEGs) in different clusters. Bonferroni correction method was used to adjust p value, and DEG with p value larger than 0.05 after correction was eliminated. The nonparametric Wilcoxon rank sum test in the "Seurat" software package was used to analyze the differential expression between subsets.

### Cell cycle and differentiation analysis

Cells in each spot were divided into specific cell cycle and differentiation stage based on G2/M and S related gene expression (Table S2) and cell differentiation states (epithelium, p-EMT; Table S3). Briefly speaking, we used the "CellCycleScoring" and "AddModuleScore" function to calculate the cell cycle and differentiation score of each spot, and then matched it to the metadata.

### Trajectory, pseudo-time, and immune analysis

The "Monocle2" software is used to identify differential genes that change between clusters or spots for developmental trajectory and pseudo-time analysis. The "Monocle2" package for trajectory and pseudo-time analysis contained 400 marker genes from the "differentialGeneTest" function that is designed to infer potential pedigree differentiation trajectories. A generalized additive model (GAM) is constructed to generate the average expression of each isotype. RNA counts of all spots in the cluster were selected as the input of "Monocle2" for downstream analysis. Additionally, we also used "AddModuleScore" function to evaluate the feature scores for immune infiltration enrichment based on the specific markers for T cells. B cells, NK cells and myeloid cells (Table S4).

## Results

### General profiles of spatial transcriptomics sequencing in hepatocellular carcinoma

To systematically explore the relations between spatial expression patterns and tumor heterogeneity in hepatocellular carcinoma, we randomly sampled tissues from two regions of surgically resected and pathologically confirmed HCC (HCC-R1, R2) of the same case with clearly demarcated and continuous cores, peripheral regions, and boundary regions. The fresh-frozen samples were then subjected to spatial transcriptomics sequencing via the 10× Genomics Visium platform with histological staining, cDNA sequencing library preparation, and further sequencing procedures. Hematoxylin-eosin staining revealed histological locations and boundaries; thus, we annotated them as sectors of carcinoma, para-carcinoma and fiber cord based on spatial locations (Figure 1A). We first integrated two samples and obtained 7553 specific captured areas (spots) on the ST arrays. Each spot reaches a length of 55 μm and contains a mixture of several cells that are not necessarily of the same cell type, which serves as an individual unit for further computational analysis and visualization. Data also showed that the mean number of nCount per spot was 22,387, and the mean gene count was 4,321 in this study, which qualified the sequencing data.

Next, we performed hierarchical clustering, and all the spots were further yielded into 15 clusters. We also investigated the spatial distributions of 15 clusters and nCounts among two samples. Generally, certain clusters (HC- 01, 02, 04, 07, 08, 09, 10, 12, 14, and 15) were in the carcinoma sector, while clusters (HC-03, 05, 06, and 12) were in the para-carcinoma sector and cluster HC-11 was in the fiber cord sector.

It was also obvious that the number of nCounts in the carcinoma sector was larger than that in the para-carcinoma region and fiber cord sector, revealing a high abundance of gene expression in the tumor region (Figure 1A). All these clusters in the carcinoma sector indicated more nCounts than the clusters from other sectors (Figure 1B), which reflected a hyperproliferative state in the tumor region and was consistent with the results reported in previous studies [25]. Uniform Manifold Approximation and Projection (UMAP) dimension reduction analysis depicted clear spatial segregation of spots belonging to specific clusters from the carcinoma, fiber cord and para-carcinoma sectors as the distance between the points represents the similarity between spots and spots of the same can form clustering, while spots of different clusters or subsets have obvious separation (Figure 1C), which further confirmed that various spatial regions cannot only be defined by histological assessments but also can be specifically distinguished from one another by spatial gene expression patterns. We displayed the distribution of 15 clusters among two samples and the results demonstrated that almost all the clusters existed in two samples. However, the proportion of the same cluster among two distinct samples are quite heterogeneous due to the discrepancy of spatial locations (Figure 1D).

To further characterize the identified clusters, we performed differentially expressed gene (DEG) analysis and profiled the featured DEGs in each cluster at the set of log-fold change (log FC) thresholds of 0.25 (Figure S1A). We examined the spatial expression of marker genes previously reported for common cell types in two samples to assess the sensitivity of the method of detecting the transcripts per spot, and the results confirmed that *ALB* and *CYP2E1* [14] were highly expressed in para-carcinoma regions; *GPC3* [26] and *AKR1B10* [27] in carcinoma regions; *ACTA2* and *COL1A1* (markers typically associated with activated fibroblasts or cancer-associated fibroblasts) [28] in the fiber cord and stromal regions, and the above also confirmed the reliability of ST sequencing results. We also detected the spatial distribution of *PTPRC* (leukocyte marker) [29], *CD2* (T cell and NK cell marker) [30], and *LYZ* (myeloid cell marker) [31] in two samples (Figure 1E); however, no evident spatial characteristics of these markers were found.

In the multi-step process of tumorigenesis, the basic biological functions of tumor cells have altered, such as the acquisition of unlimited replication and colonization ability and the activation of metastasis and invasion capacity [32]. Consequently, we evaluated each spot or cluster for its likely cell cycle phases using signatures defined for G1, S, and G2/M phases based on functional annotations (Table S2). We found that most of clusters from the carcinoma sector had a higher proliferative capacity compared with those from the para-carcinoma and fiber cord sector (Figure S1B). We also appraised the differentiation origins of each cluster and undoubtedly found that the cluster HC-11 from fiber cord sector dominated the mesenchymal differentiation scores. Strikingly, clusters (HC-07, 08, and 09) originating from mesenchymal differentiation were situated in carcinoma sectors, revealing the epithelial-mesenchymal transition (EMT) process and potential malignancy of these carcinoma clusters (Figure S1B; Table S3).

Taken together, our recent analysis of spatial transcriptomics on two sections of HCC samples preliminarily reveals the discrepancies of gene expression patterns within the different regions of HCC microenvironment, providing new insights and novel strategies for exploring the relations between spatial gene expression and tumor heterogeneity of HCC.

## The spatial expression pattern of CCL15 in the tumor core region facilitates the HCC immunosuppressive microenvironment

Next, we intended to elaborate the spatial expression pattern and underlying mechanisms in distinct sectors. We set out to assess the differentiation and development trajectory of spots in the carcinoma sector using pseudo-time analysis and observed the developmental trajectory among clusters in HCC-R1/R2 (Figure 2A). Notably, clusters (HC- 01, 10, 14, and 15) were in the end stage of the developmental trajectory in HCC-R1/R2. All these clusters were also spatially located in the internal area of the carcinoma sector with the highest nCount, as shown before; hence, we annotated them as the core region of the carcinoma sector and displayed them among two samples (Figure 2B).

Subsequently, we speculated that inherent regularity of gene expression existed, especially in the core regions. We then analyzed and marked the top 20 DEG genes in tumor core regions and found that *IGHG1*, *IGHG3*, *IGHG4*, *IGKC*, and *IGLC2* (effector markers for humoral immunity) were notably downregulated in core regions, possibly indicating an immunosuppressive microenvironment (ISME). Among the upregulated genes presented, most of them (NUPR1, GSTA2, CCL15, UQCRH, GAPDH, and so on) have been documented previously to be elevated in HCC and play oncogenic roles in various aspects (Figure 2C) [33-36]. Further analysis revealed that those downregulated genes were mainly expressed at the early stages in the trajectory of clusters from HCC-R1/R2 and diminished as the

pseudo-time progressed, with the lowest expression at the end stage; however, nearly all the upregulated genes conversely increased gradually, and most of them were expressed in the end stages of the trajectory (Figure 2D). Interestingly, *IGHG1*, *IGHG3*, *IGHG4*, *IGKC*, and *IGLC2* were deficient at the end states of time, thus facilitating an immunosuppressive microenvironment (Figure 2E), while the reason why they were formed was unclear. Among those genes that dominated at the end of development trajectory, we noted that *CCL15*, an oncogenic chemokine, accumulated along the pseudo-time trajectory and was identified to facilitate the formation of tumor ISME (Figure 2E).

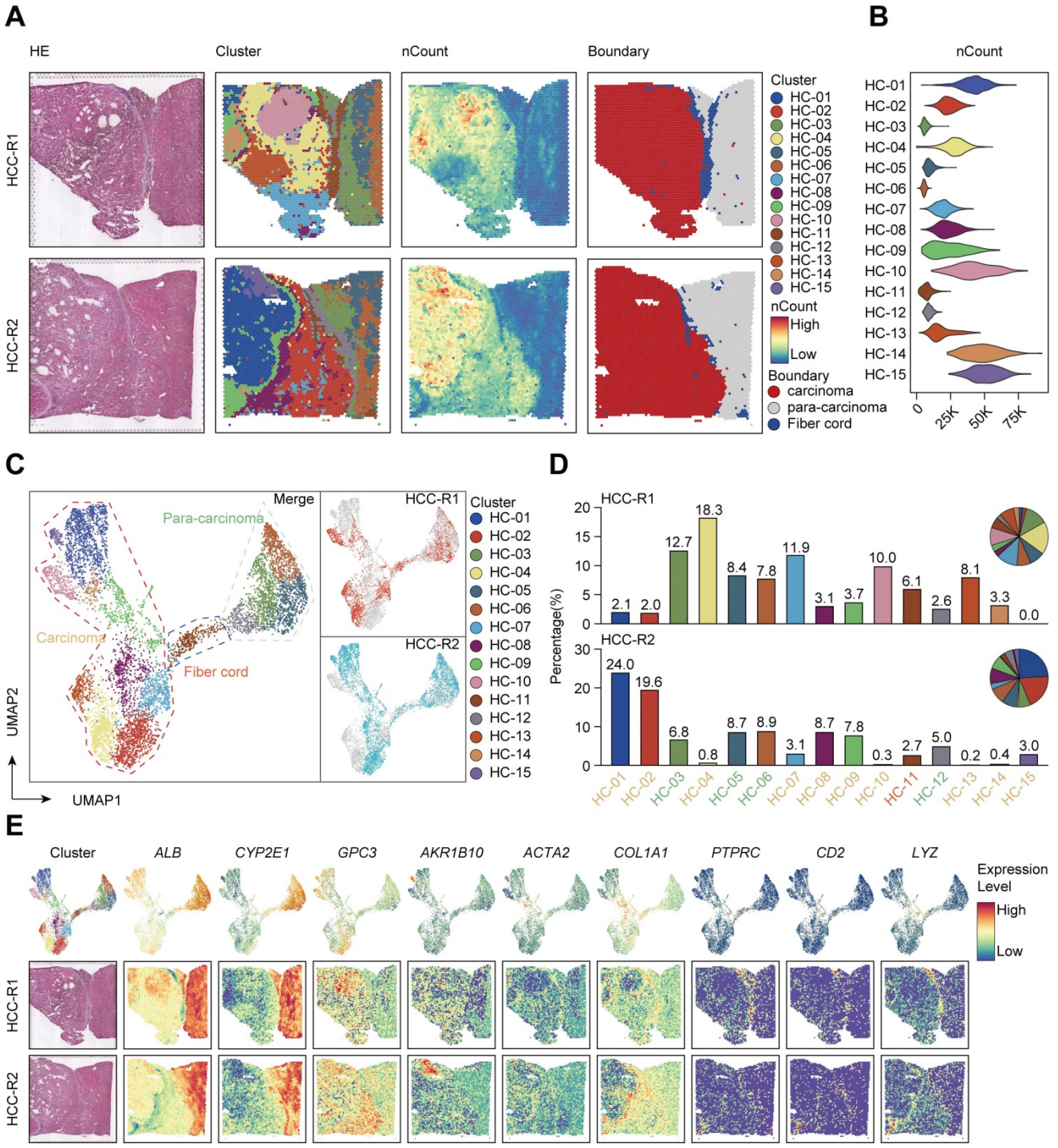


**Figure 1. Overall landscapes of spatial transcriptomics in hepatocellular carcinoma. A.** Spatial distribution of 15 clusters and nCounts as well as histological assessment and boundary among two regions of HCC (HCC-R1, R2). **B.** Violin plot demonstrating the number of UMI counts in 15 clusters. **C.** UMAP plot of all the spots from 15 clusters (colored by clusters and spatial locations; orange represents carcinoma, green represents para-carcinoma and red represents fiber cord). **D.** Bar plot showing the distribution of each cluster among two samples and pie plot indicating the proportion of clusters in each sample. **E.** Hematoxylin-eosin staining and spatial feature plots of marker genes in each sample.

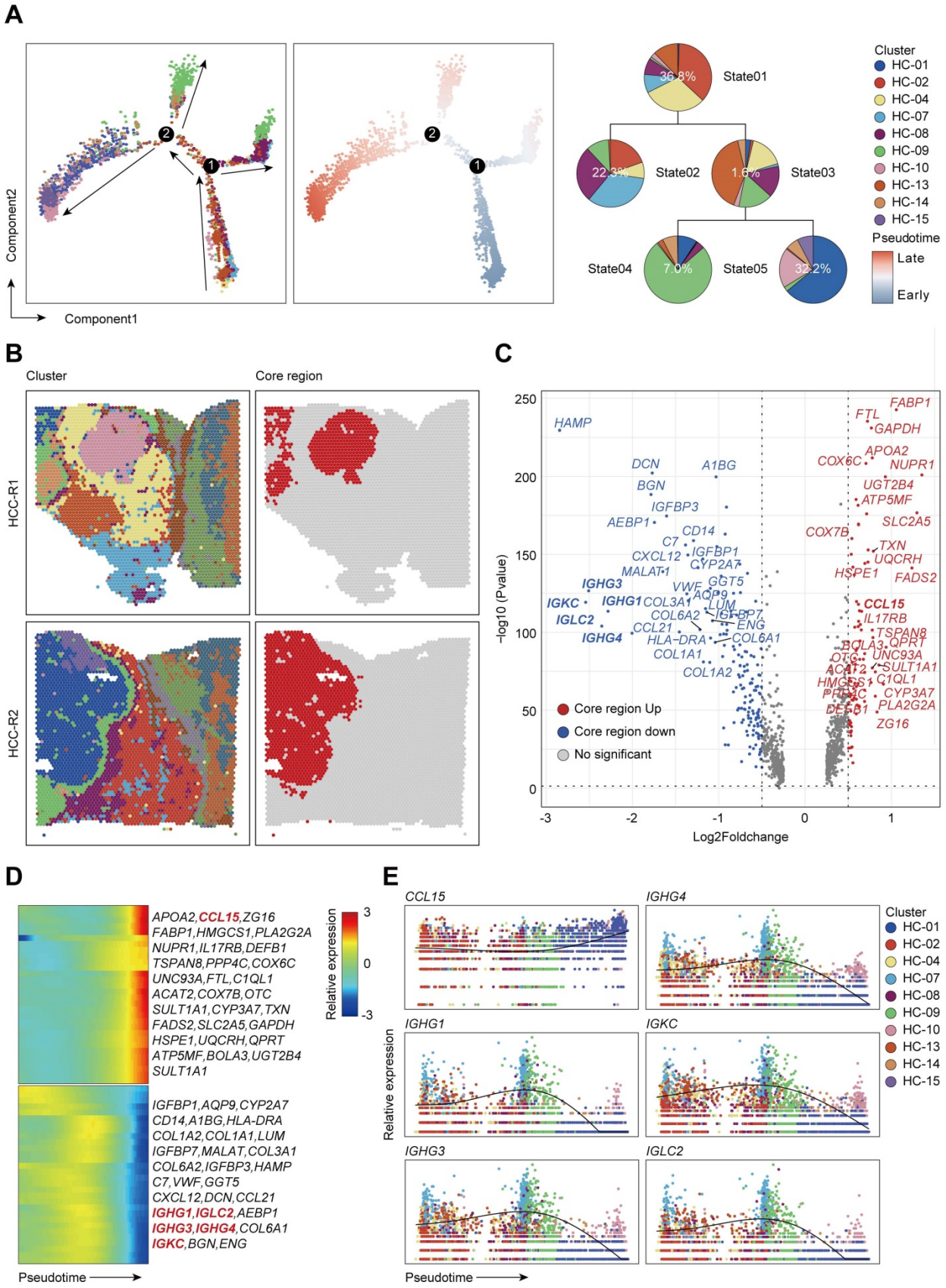


**Figure 2. The spatial expression pattern of CCL15 in the tumor core region facilitates the HCC immunosuppressive microenvironment. A.** Pseudo-time analysis and pie plots showing the developmental trajectory of spots from HCC-R1 & R2, colored by the clusters, states and pseudo-time. **B.** Spatial distributions of clusters in R1 & R2 as well as in the core region of HCC. **C.** Volcano plot of significantly differentially expressed genes in the core region of HCC. **D.** Heatmap displaying expression changes of differentially expressed genes in HCC-R1 & R2 along the pseudo-time trajectory. **E.** Scatter plots and fitting curves presenting the expression trend of selected marker genes in HCC-R1 & R2 along the pseudo-time trajectory.

Given the limits of tissue samples, we further performed a secondary data analysis on a previous study of ST sequencing on primary liver cancers, which also presented spatial transcriptome map of three major liver cancer subtypes [23]. In order to better match the spatial location of our tissue samples with higher spatial continuity that includes the carcinoma, fiber cord sector to para-carcinoma sector, we chose the leading-edge section of 4 HCC samples from their ST data and annotated them as HCC1, HCC2, HCC3, and HCC4 (Figure S2A). We reappraised histological boundaries, nCount profiles and performed clustering analysis on each tissue separately. We displayed spatial distributions of all the clusters among each tissue and HCC-1/2/3/4 can be clustered into 11, 9, 12, and 9 clusters, respectively. Notably, the number of nCounts in the carcinoma sector was remarkably larger than that in other sectors (Figure S2A). We also presented the spatial features and relatively quantified the levels of *CCL15* among 4 samples, which revealed that *CCL15* was obviously upregulated in the carcinoma sector of HCC1 and HCC4, however, no distinct and similar difference in HCC2 and HCC3 was observed (Figure S2B-C). Hence, we further analyzed the developmental trajectory of specific clusters pertaining to carcinoma sectors among HCC1 and HCC4 as previous mentioned (Figure S3A-B). *CCL15* was also increased as the pseudo-time progressed and was dominant in the end stages of the pseudo-time axis; Conversely, other key molecules such as *IGHG1*, *IGHG3*, *IGHG4*, *IGKC*, *IGLC2* decreased gradually among all the carcinoma sectors in HCC1 and HCC4 (Figure S3C-D). Taken together, their ST data on 4 pieces of HCC samples with spatial continuity supported our core conclusions and CCL15 did contribute to facilitating the HCC immunosuppressive microenvironment.

## CCL15 recruits and polarizes M2-like macrophages *in vitro* and *in vivo*

Since the chemokine CCL15 was crucial for HCC immune microenvironment, we wondered how did CCL15 contribute to the formation of an immunosuppressive microenvironment that accordingly affected clinical outcome of HCC patients. To better investigate the potential mechanism of CCL15, we found that CCL15 was the most highly expressed in liver cancer among 21 solid tumors from the TCGA data (Figure S4A), indicating that CCL15 may play important roles in the progression of the liver tumor microenvironment (TME). Previous studies have shown that CCL15 can recruit $CCR1^+$ bone marrow-derived inhibitory cells and $CCR1^+$ neutrophils to promote liver metastasis of colorectal cancers [37-39]. In another study, CCL15 can recruit suppressive $CCR1^+CD14^+$ monocytes into HCC tissues and promote immune escape by upregulating the expression of PD-L1, B7-H3, and IDO and activating STAT1/3, AKT, ERK, and other signaling pathways in an autocrine manner to promote HCC progression [35]. We also analyzed their comparison data and found that $CCR1^+CD14^+$ monocytes recruited by CCL15 showed significantly higher expression levels of the M2-like macrophage markers *CD163L1* and *CD200R* [35], suggesting the potential of $CCR1^+$ monocytes recruited by CCL15 to polarize toward the M2-like type. Importantly, we observed a positive correlation between CCL15 and the infiltration degree of M2-like macrophages in the TIMER database (Figure 3A). M2-like macrophages secrete various growth factors, cytokines, and collagenases and consequently promote tumorigenesis and tumor development [40]. Taken all these standpoints into account, we hypothesized that CCL15 may be associated with M2-type macrophages and synergistically facilitate the immunosuppressive microenvironment of HCC. To verify the hypothesis, we next constructed macrophage models *in vitro* with THP-1 or U937 cell lines stimulated by phorbol ester (PMA), which increases the expression of macrophage markers (Figure S4B). After pre-experimentation to determine the optimal stimulating concentration of CCL15 (Figure S4C-D), we found that the markers of M2-like macrophages and their receptor CCR1 were upregulated at both the transcript and protein levels (Figure 3B-E). Flow cytometric analysis showed that the proportion of $CD163^+CD206^+$ positive cells increased compared to the control group after CCL15 stimulation, revealing a trend of macrophage polarization toward the M2-like type (Figure 3F-G). Furthermore, transwell migration assays showed an enhancement in the migration ability of macrophages in the presence of CCL15, indicating that CCL15 enhances the chemotaxis capacity of macrophages (Figure 3H-I). To verify the results *in vivo*, we also propagated massive Huh7 cells overexpressing CCL15 stably and applied subcutaneous tumorigenesis model with nude mice. We found that overexpressing CCL15 can increase the vitality and tumor growth of xenograft tumors (Figure 3J, Figure S4E-F). Intriguingly, the expression of CD163 in the overexpressing group was higher than that in the control group, revealing a higher infiltration of CD163 macrophages in the xenograft tumors after overexpressing CCL15 (Figure 3K). Collectively, these observations demonstrated that CCL15 can recruit monocytes and polarize them toward M2-like macrophages *in vitro* and *in vivo*, but further mechanism study is still demanding.

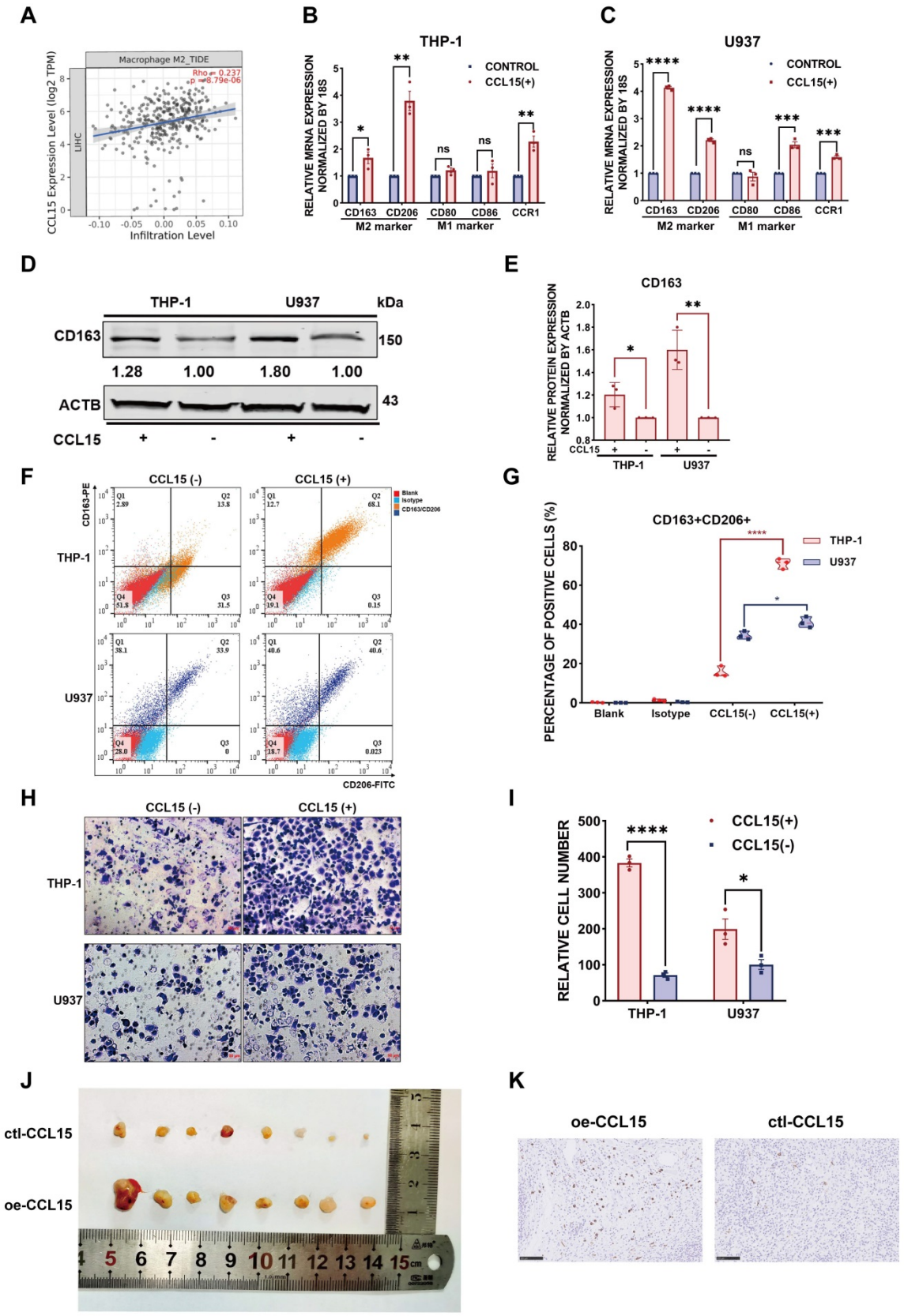


**Figure 3. CCL15 recruits and polarizes M2-like tumor-associated macrophages *in vitro* and *in vivo*. A.** Correlation between expression of CCL15 and infiltration of M2-like macrophages from the TIMER database. **B-C.** Relative mRNA levels of macrophage markers (M1, M2) and *CCR1* after treatment with CCL15 in THP-1 (**B**) or U937 (**C**) cells. **D-E.** Immunoblotting image (**D**) and relative quantitative analysis (**E**) of the M2-like macrophage marker CD163 after treatment with CCL15 in THP-1 and U937 cells. **F-G.** Flow cytometric image (**F**) and relative quantitative analysis (**G**) revealing the percentage of $CD163^{+}CD206^{+}$ M2-like macrophages after treatment with CCL15. **H-I.** Representative image (**H**) and quantitative result (**I**) of transwell migration assay of monocytes from THP-1 and U937 cells after treatment with CCL15 (scale bar, 50 μm). **J.** Representative image of subcutaneous xenografts resected from the oe-CCL15 group and control group. **K.** Immunohistochemical analyses of CD163 in the oe-CCL15 group and control group (scale bar, 100 μm).

## Combined predictive role of CCL15 and CD163 in the worse prognosis of HCC patients

Additionally, we further detected the expression of CCL15 and the M2-like macrophage marker CD163 in HCC tissues of 89 patients from the CH cohort (Figure 4A). The results indicated a positive correlation (R=0.4367, p<0.0001) between CCL15 and CD163 expression levels (Figure 4B). After determining the optimal cutoff values using X-tile software (Version 3.6.1), both CCL15 and CD163 correlated significantly with prognosis, and the higher the levels of CCL15 or CD163 were, the worse the OS and RFS of the patients (Figure 4C-F). Furthermore, the combined predictive value of CCL15 and CD163 was higher, with an area under the curve (AUC) of 0.68/0.79 for one/five years of OS, than that of CCL15 alone (AUC area of 0.63/0.75) and CD163 alone (AUC area of 0.64/0.69) (Figure 4G-H), which indicated the superior value of them in predicting the prognosis. Therefore, we further evaluated the relationship between combined application of the CCL15 and CD163 expression and the prognosis of HCC patients. Based on the expression differences, all the patients can be classified into $CCL15^{hi}CD163^{hi}$ group, $CCL15^{hi}CD163^{lo}$ group, $CCL15^{lo}CD163^{hi}$ group, $CCL15^{lo}CD163^{lo}$ group, respectively. We next compared the relationship of survival prognosis among these four groups, and found the most significant survival difference between the $CCL15^{lo}CD163^{lo}$ group and the $CCL15^{hi}CD163^{hi}$ group. $CCL15^{hi}CD163^{hi}$ group was blessed with the worst prognosis, verifying the predictive superiority of joint application of CCL15 and CD163. The five-year survival rate (14.29%) and median survival time (35.83, 95% CI: 25.37–46.28) for OS and the five-year survival rate (2.85%) and median survival time (24.34, 95% CI: 16.13–32.55) for RFS of the $CCL15^{hi}CD163^{hi}$ group were the worst among the four groups (Figure 4I-J). However, we did not observe obvious significance in the clinical characteristics between the $CCL15^{hi}CD163^{hi}$ and $CCL15^{lo}CD163^{lo}$ groups due to the limits of sample capacity (Table S5).

Taking the above results into account, our results suggest that CCL15 may promote the formation of immunosuppressive microenvironment and affect the prognosis of HCC patients by recruiting and polarizing M2-like macrophages. Furthermore, the high expression of CCL15 and M2-type macrophage marker CD163 predicts poor survival prognosis, and the combined application of CCL15 and CD163 expression has better prognostic value. These results further enrich the function and role of CCL15 in the immune microenvironment of HCC, but the mechanisms driving tumor progression by CCL15 and M2-likes macrophages still need further discussion.

## CCL19 and CCL21 share similar expression patterns and are remarkable in the immune infiltration enrichment (IIE)

Given that cellular components of tumor microenvironment are fairly complex, with distinct populations of immune cells playing vital roles in the progression of HCC as well as immunotherapy, recent studies have tried to elaborate the characteristics and functions of T cells, tumor-associated macrophages (TAMs), and dendritic cells (DCs) in HCC [11, 12], but the global landscapes of immune cells are still poorly understood. In our studies, we first scored the abundance of immune cells such as T cells, B cells, natural killer cells, and myeloid cells annotated by cell marker signatures (Table S4) among 15 clusters (Figure 5A) and characterized the spatial expression patterns of immune cells among two samples (Figure 5B). T cells and B cells seemed to be remarkably infiltrating in specific areas or clusters among the tissues; NK cells presented a low abundance in HCC and spatially localized in a random regularity; Myeloid cells were the most abundant immune cells but without apparent discrepancy in spatial distributions due to the limits of sequencing length, and consequently we cannot distinguish specific myeloid subsets such as monocytes, macrophages and other cell types (Figure 5B). After hierarchically clustering the abundance of immune cells, clusters (HC-09, and 11) were notably enriched with immune cells compared with other clusters and were well integrated together, which indicated the most enrichment of immune cells such as T cells, B cells and myeloid cells (Figure 5C); thus, we defined the aggregation of these clusters as immune infiltration enrichment (IIE).

We investigated the significantly upregulated genes in the IIE and observed that *IGHG1*, *IGHG3*, *IGHG4*, *IGLC2*, *IGKC*, *IGHA1*, *IGHM* and other molecules were dramatically elevated (Figure 5D), which in turn confirmed the aggregation of B cells in these clusters (Figure 5A-C). However, we still wondered what triggered the accumulation of immune cells in the IIE. We noticed that *CCL19* and *CCL21* were also obviously prominent among the upregulated genes. Both CCL19 and CCL21 are derived from a population of identical cells, such as various stromal cells within primary and secondary lymphoid organs, T lymphocytes, and lymphatic endothelial cells, in peripheral tissues [41]. CCL19 and CCL21 are mainly involved in the homing, migration process and maturation of dendritic cells, as well as in the activation, recruitment and recirculation of T

lymphocytes and B cells in the adaptive immune system [42, 43]. Moreover, several studies have indicated that CCR7-CCL19/CCL21 has an antitumor function by recruiting T lymphocytes and dendritic cells in lung cancer and other malignant tumors [44, 45], and few have been reported in HCC yet. We therefore hypothesized that upregulated CCL19 and CCL21 may be the leading cause of the enrichment of immune cells in the IIE. We further detected the expression levels and spatial distribution of *CCL19* and *CCL21* among 15 clusters and two pieces of samples (Figure 5E-F). In accordance with previous results, *CCL19* and *CCL21* shared similar spatial expression patterns, and both were mainly in the fiber cord sector (Figure 5F). Although the expression of *CCL21* was much higher than that of *CCL19*, *CCL19* was positively correlated with *CCL21* among 15 clusters in two samples (Figure 5G).

To comprehensively demonstrate the functions of CCL19 and CCL21 among immune micro-environment, we further investigated the expression levels and spatial distributions of *CCL19* and *CCL21* among the clusters from the leading edging section of 4 pieces of HCC samples from our secondary data analysis (Figure 6A-B) on previous ST data [23]. We also detected the infiltration degrees and spatial distributions of immune cells and observed that T cells and B cells were mainly enriched in the fiber cord sector (Figure 6C-D), which is in accordance with the spatial expression patterns of *CCL19* and *CCL21*. After hierarchically clustering the abundance of immune cells, we further defined the IIE among 4 samples (Figure 6E). Consistent with our ST data, *CCL19* and *CCL21* were dominant in the up-regulated genes among the IIE (Figure 6F). Furthermore, the level of *CCL19* was positively correlated with CCL21 among the clusters from 4 samples respectively (Figure 6G). Conclusively, CCL19 and CCL21 may also function in synergistic effects on biological processes among the IIE region in the spatial architecture of HCC due to their similarity in spatial expression patterns and interactive approaches, which was reliably confirmed by previous ST data as well.

## CCL19 and CCL21 inhibit the growth of HCC by enriching the abundance of T cells and B cells

Considering their similarities in spatial expression patterns in our ST data, we have strikingly verified their positive correlation from our second data analysis (Figure 6G), which was also strongly confirmed with a coefficient of 0.99 from the TCGA database (Figure 7A), reflecting a potential synergistic effect between CCL19 and CCL21. Moreover, we analyzed the predictive roles in prognosis with combined CCL19 and CCL21 in HCC and observed that high expression of CCL19 and CCL21 predicts a good prognosis in liver cancer from the TCGA database (Figure S5A), suggesting that combined CCL19 and CCL21 may be used as a new strategy for HCC immunotherapy. To evaluate the potential therapeutic effects and possible mechanisms, we next constructed vectors of adeno-associated viruses (AAV-8) overexpressing *Ccl19*, *Ccl21a* and combined *Ccl19*/*Ccl21a*, which target hepatic cells specifically, and evaluated therapeutic effects in the subcutaneous xenograft models respectively. Results showed that overexpressing combined *Ccl19*/*Ccl21a* can remarkably retard tumor growth and decrease tumor vitality of hepa1-6 cells, while overexpressing *Ccl19* or *Ccl21a* alone showed a slightly significant difference of tumor growth compared to the control group (Figure S5B-D), indicating that overexpressing combined *Ccl19* and *Ccl21a* elicited a synergistic effect in inhibiting the tumor growth. Hence, we next focused on the combined therapeutic effects of *Ccl19*/*Ccl21a* with further research. Besides subcutaneous tumor models, we also built DEN/$CCl_4$-induced liver cancer models, and the timeline and procedures are shown (Figure S5E). Specifically, we chose C57/BL6 mice rather than SCID or nude mice for the experiments due to the deficiency in normal immune functions of the latter types.

In the subcutaneous xenograft model, hepa1-6 cells were first injected into the bilateral armpits of 24 mice, and the growth of emerging tumors was dynamically monitored every four days. Ccl19/Ccl21a-overexpressing AAV (oe-AAV) and control AAV were then intratumorally injected when the largest diameter of the xenograft reached 5 mm. The results showed that the growth of tumors from the oe-AAV group was slowed and the tumor volume was gradually reduced, whereas the tumor growth and tumor volume of the control AAV group continued to increase (Figure 7B). The weight and volume of tumors in the oe-AAV group were smaller than those in the control group (Figure 7B-D), indicating that CCL19 and CCL21 have a therapeutic effect in inhibiting the growth of HCC. Previous studies showed that CCL21 can affect tumor progression by recruiting immune cells such as T lymphocytes [46, 47], and have reported that tumor-infiltrating B cells may inhibit liver cancer progression and improve prognosis by interacting with $CD4^+$ T cells in close proximity and subsequently activating $CD8^+$ T cells, but the origins of tumor-infiltrating T cells and B cells are still unclear. Therefore, we hypothesized that CCL19 and CCL21 influenced the infiltration degree of T cells and B cells via recruitment.

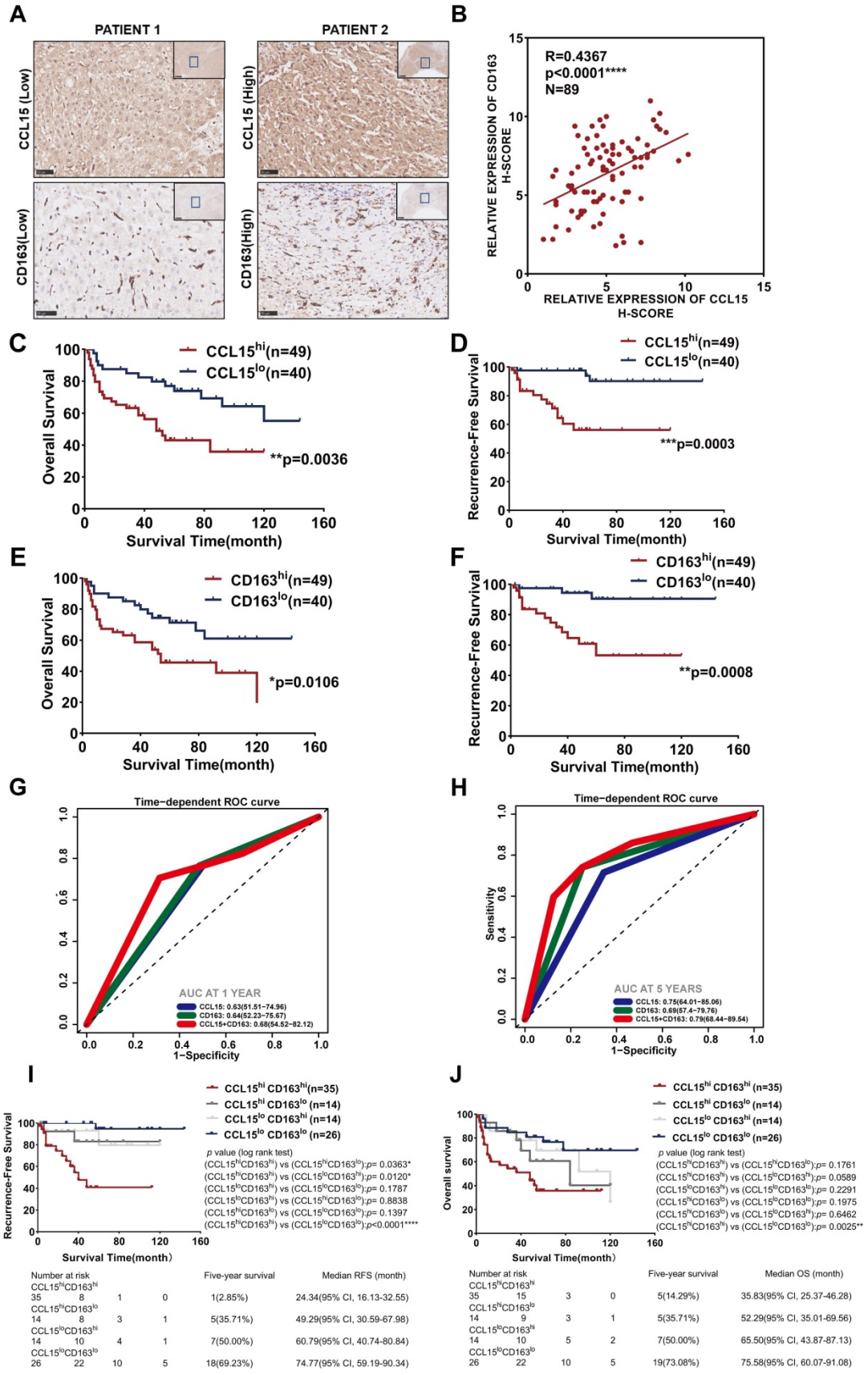


**Figure 4. Combined predictive roles of highly-expressed CCL15 and CD163 predict the worst prognosis of HCC patients. A.** Representative immunochemical staining of CCL15 and the M2-like macrophage marker CD163 in 89 patients (scale bar, 50 μm). **B.** Correlation between the relative expression of CCL15 and CD163 using the H-score method. **C-D.** Kaplan-Meier survival curves showing correlation between CCL15 alone and OS (**C**) and RFS (**D**). **E-F.** Kaplan-Meier survival curves showing correlation between CD163 alone and OS (**E**) and RFS (**F**). **G-H.** ROC analyses showing combined predictive value of CCL15 and CD163 for OS at 1 year (**G**) and 5 years (**H**). **I-J.** Kaplan–Meier survival curves showing the worst OS (**I**) and the worst RFS (**J**) in the CCL15$^{high}$CD163$^{high}$ group.

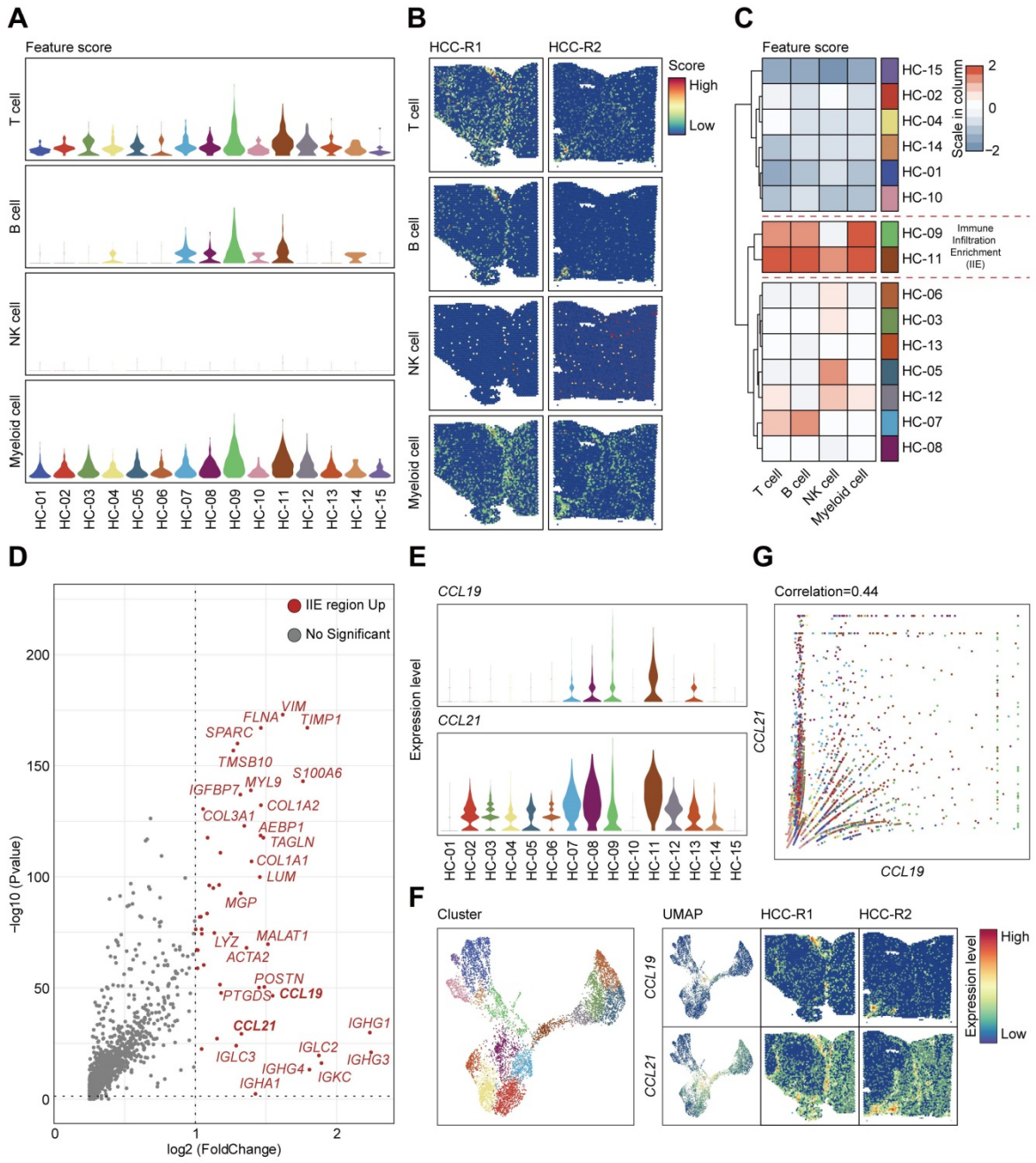


**Figure 5. CCL19 and CCL21 sharing similar expression patterns and remarkable in immune infiltration enrichment (IIE) contribute to the abundance of immune cells in HCC. A.** Violin plots showing the feature scores of immune cells such as T cells, B cells, NK cells and myeloid cells among 15 clusters. **B.** Spatial distribution of T cells, B cells, NK cells and myeloid cells in two samples. **C.** Heatmap indicating the overall infiltration of immune cells in each cluster. **D.** Volcano plot of significantly upregulated genes in the IIE. **E.** Violin plots showing the expression levels of CCL19 and CCL21 among 15 clusters. **F.** Spatial features of CCL19 and CCL21 in two samples. **G.** Correlation between the relative expression of CCL19 and CCL21 among 15 clusters.

We first evaluated relations between the levels of CCL19 and CCL21 and infiltration of immune cells in the TIMER database and found that CCL19/CCL21 correlated positively with $CD4^+$ T cells, $CD8^+$ T cells and B lymphocytes (Figure S5F), particularly with naïve T cells, central memory T cells, effector T cells and Th-1-like cells (Figure S5G, other data not shown). We further validated the correlation of *Ccl19* with *Cd3e*, *Cd4*, *Cd8a*, *Cd19*, *Cd20*, and *Ifng* (another marker of T cell activation) in subcutaneous xenografts, and the results showed that *Ccl19* correlated positively with *Cd3e*, *Cd19*, *Cd20*, and *Ifng* (Figure S5H). Furthermore, the T cell marker CD3 and the B cell marker CD20 were upregulated at the protein level in the oe-AAV group compared to the control group (Figure 7E-F). Flow cytometric analyses of tumor xenografts revealed a higher proportion of $CD3^+$ cells and $CD20^+$ cells in the oe-AAV group than in the control group (Figure 7G-H), and tissue immunofluorescence results confirmed significantly higher infiltration of $CD3^+$ T cells and $CD20^+$ B cells in the oe-AAV group (Figure 7I).

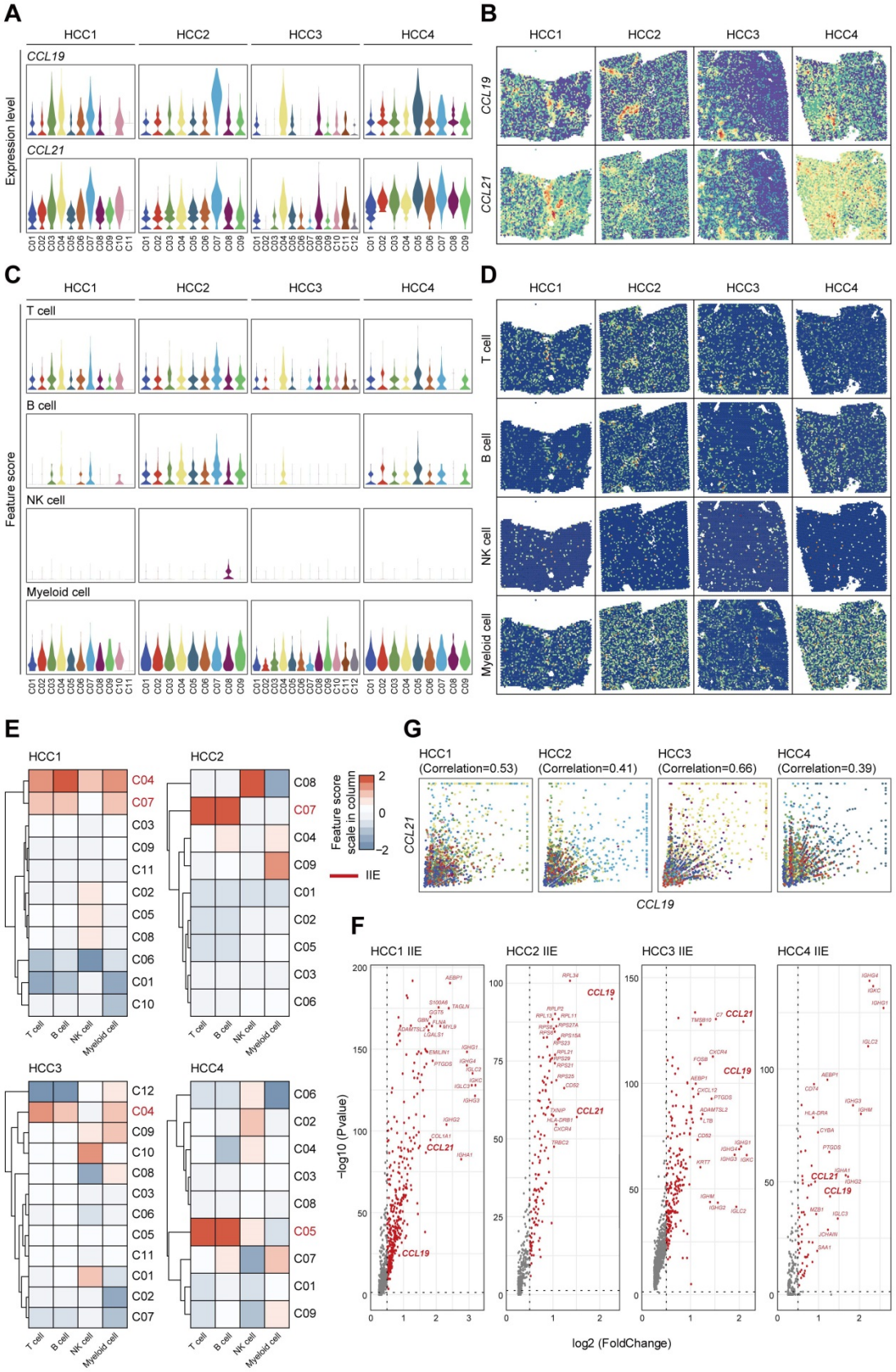


**Figure 6. Highly-correlated CCL19 and CCL21 are indeed dominant in the IIE from secondary data analysis of previous ST sequencing on HCC. A.** Violin plots showing the expression levels of *CCL19* and *CCL21* among all the clusters from four various samples. **B.** Spatial distribution of *CCL19* and *CCL21* among four samples. **C.** Violin plots showing the feature scores of immune cells such as T cells, B cells, NK cells and myeloid cells among all the clusters from four various samples. **D.** Spatial distribution of T cells, B cells, NK cells and myeloid cells among four samples. **E.** Heatmap indicating the overall infiltration of immune cells in each cluster and the IIE in each sample (the clusters marked red). **F.** Volcano plot of significantly upregulated genes in the IIE among four samples. **G.** Correlation between the relative expression of CCL19 and CCL21 in all the clusters among each sample.

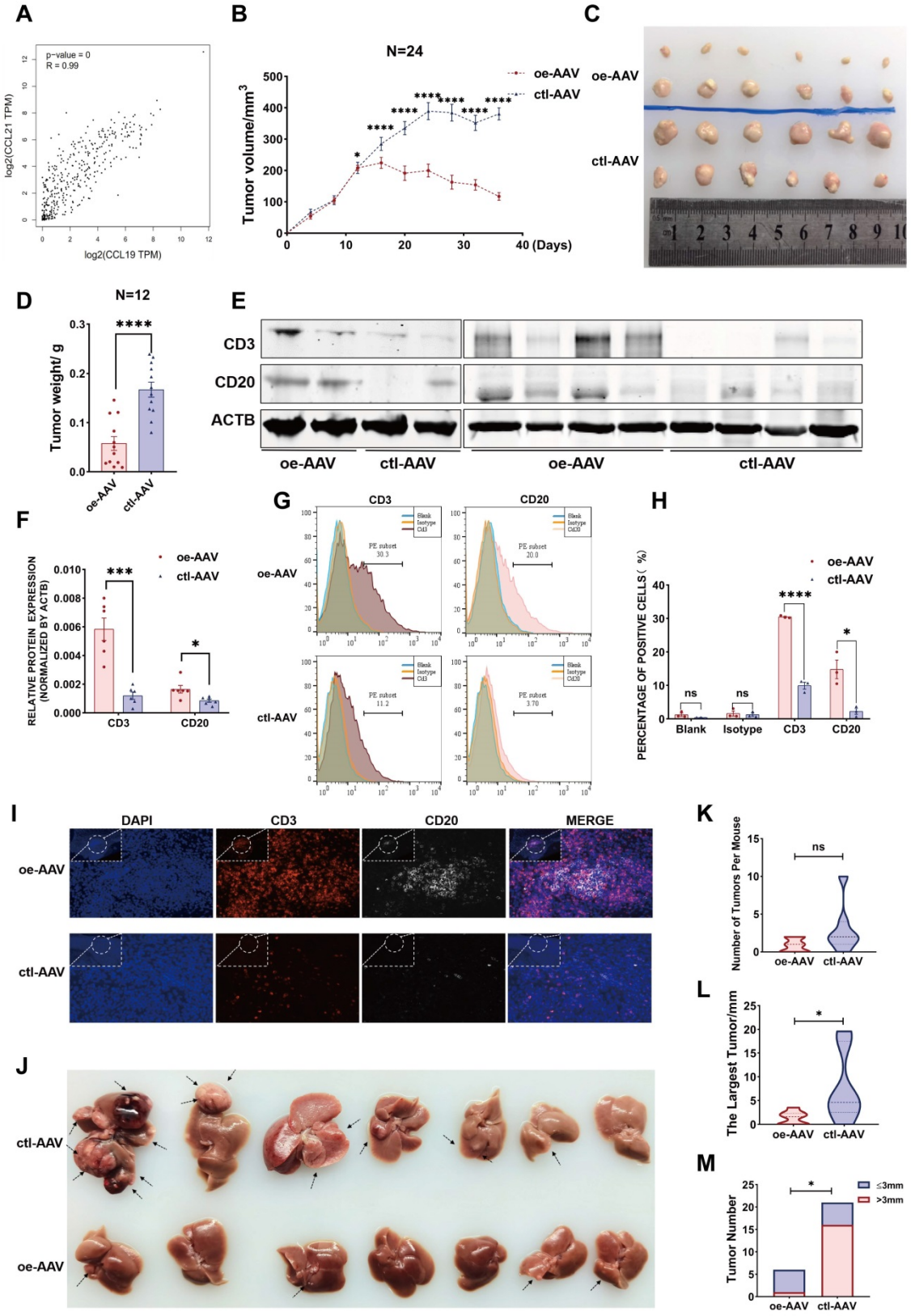


**Figure 7. CCL19 and CCL21 inhibit the growth of HCC by enriching the abundance of T cells and B cells. A.** Correlation between expression of CCL19 and CCL21 in HCC from TCGA database (R=0.99. p-value=0). **B.** Tumor volume changes of subcutaneous xenografts after hepa1-6 cell clones were implanted, n=24. **C.** Representative image of subcutaneous xenografts resected from the oe-AAV group and control group (n=12). **D.** Tumor weight of subcutaneous xenografts from the two groups. **E-F.** Immunoblotting image (**E**) and relative expression (**F**) showing CD3 and CD20 in subcutaneous xenografts of the two groups (n=6). **G-H.** Flow cytometric image (**G**) and relative quantitative analysis (**H**) indicating $CD3^+$ and $CD20^+$ cells in the two groups. **I.** Immunofluorescence image showing the infiltration of $CD3^+$ T cells and $CD20^+$ B cells in the two groups (scale bars 20 μm; 10 μm). **J.** Resected liver image showing tumor growth of DEN/$CCl_4$-induced HCC after tail vein injection of AAV (n=7). **K.** Comparison of total tumor number between the oe-AAV group and the control AAV group from DEN-$CCl_4$-induced HCC models. **L.** Comparison of the largest tumor diameters between the two groups. **M.** Comparison of the number of tumor diameters (>/≤3 mm) between the two groups.

In another model, mice were tail vein injected with oe-AAV and control AAV after DEN/$CCl_4$-induced liver tumors arose, and the mice were sacrificed after three months (Figure 7J). The results indicate no significant difference in the overall tumor number (Figure 7K), while the maximum tumor volume and the number of tumors larger than 3 mm were conspicuously reduced in the oe-AAV group compared with the control AAV group (Figure 7L-7M). Taken together, these observations indicate that CCL19 and CCL21 inhibit the growth of HCC by enhancing the infiltration of tumor-infiltrating T cells and B cells. Thus, overexpression of *Ccl19*/*Ccl21a* AAV may be used as a novel strategy for immunotherapy of HCC, but further analysis is essential.

## Discussion

HCC is a highly heterogeneous and malignant tumor, and the relationship between HCC heterogeneity, microenvironment and spatial location has been widely discussed [23, 48, 49]. Most of the previous studies have focused on the overall gene expression of mixed cells in carcinoma and para-carcinoma areas, but the accuracy of gene expression is insufficient enough for detailed and in-depth studies [22, 50-52]. As sequencing techniques advances, single cell transcriptomics can analyze the function of cell subsets at the level of single-cell resolution [14, 53], but spatial specificity of gene expression cannot be determined due to the absence of spatial information of intricate tissue structures, while spatial transcriptomics sequencing can quantify and localize gene expression, decipher the innate correlations of spatially correlated genes and accordingly tackle with this problem properly [54].

In our study, we conducted ST sequencing on two pieces of HCC specimens from one patient. Each piece of tissues comprised distinct but continuous regions from carcinoma tissue and the tumor boundary region to para-carcinoma tissue. We first described overall landscapes of spatial gene expression patterns among two samples and intratumor heterogeneity. Next, we defined the tumor core region and the IIE via bioinformatics analysis, which was also confirmed by our secondary data analysis on previous study focusing on tumor heterogeneity of primary liver cancers [23]. Finally, we further validated the analysis results through the molecular, cellular, animal experiment and clinical tissue samples, the basic conclusions are as follows: (1) All spots were categorized into 15 subgroups by hierarchical clustering, differentially expressed genes and dimension reduction analysis, and their relationship with spatial location was determined; (2) Malignant subsets with intratumor heterogeneity phenotypes were identified by nCount, cell cycle phases, and epithelial-mesenchymal feature analysis; (3) Specific immune-related spatial regions, such as the tumor core region and the IIE, were defined by the pseudo-temporal analysis of tumor subsets and spatial expression patterns of immune cells; (4) CCL15 was significantly upregulated in the tumor core region, and promoted the formation of immunosuppressive microenvironment by recruiting and polarizing M2-like macrophages *in vitro* and *in vivo*; (5) High expression of CCL15 and CD163 respectively predicts poor prognosis of HCC patients, and the combined application has better predictive value; (6) Highly-correlated CCL19 and CCL21 were synergistically upregulated in the IIE and inhibited the growth of HCC by increasing the infiltration degree of T cells and B cells.

Concretely speaking, we profiled the overall landscapes of hepatocellular carcinoma with ST sequencing and all the 7553 spots were classified into 15 clusters. We then determined the features of 15 clusters belonging to distinct sectors by virtue of the histological boundaries, marker genes and differential gene expression, cell cycle phases and differentiation origins. Intratumor heterogeneity, especially immune-ITH, has been documented to impact the clinical outcomes of HCC, which is also characterized by an increased immunosuppressive or exhaustive TME; However, spatial distribution characteristics and expression of other cell markers in the tissue structure of HCC still need further consideration, and the origins and contributing factors for ITH are still largely unknown [55]. Accordingly, we next sought to explore relations between ITH and spatial expression patterns using our ST data and found that those clusters located in the core area of the carcinoma sector are also in the end stages of the pseudo-time trajectory. Consequently, we defined these clusters as tumor core region where most of the elevated DEGs were reported previously to play oncogenic roles in HCC and those significantly downregulated genes feature with humoral immunity enhancement, which jointly facilitate the formation of immunosuppressive microenvironment. Among the upregulated genes, we noted that CCL15 may be the culprit for this condition. The above results were also verified by leading-edge tissues of four HCC section samples from our secondary data analysis on a previous study [23]. Further studies revealed that CCL15 can recruit and polarize M2-like macrophages *in vitro* and *in vivo*. Clinical relevance analysis also indicated that high expression of CCL15 or the M2-like macrophage marker CD163 predict a poor prognosis of HCC and the combined predictive value of CCL15 and CD163

in the prognosis is superior to that using either marker alone. Currently, macrophage polarization involves a variety of molecular mechanisms, including TLR4/NF-κB, JAK/STATS, TGF-β/SMADS, PPARγ, NOTCH and microRNA signaling pathways [56], however, the detailed mechanism driving M2-like macrophages by CCL15 will be our future work.

Furthermore, we also evaluated the infiltration scores and spatial distributions of various immune cells, including T cells, B cells, NK cells and myeloid cells among 15 clusters. Clustering results showed that two clusters are rich in immune cells especially T cells and B cells, and are annotated as immune infiltration enrichment. Contrary to the conditions of tumor core region, upregulated DEGs in the IIE are characterized by immunoglobin families and two prominent chemokines, CCL19 and CCL21, and the results are verified by our second data analysis on a previous study [23].

Further studies elucidated their strong correlations and similarities in spatial expression pattern, biological process and clinical significance of HCC. *In vivo* experiments of AAV showed that high expression of CCL19 and CCL21 inhibits the growth of HCC by influencing the infiltration of $CD3^+$ T cells and CD20+ B cells in the subcutaneous xenograft model, while there was a slight significance in the DEN/CCl4-induced tumor models when compared with tumor sizes in two groups. The reason may well be that CCL19 and CCL21 function better in the tumor progression rather than the tumorigenesis process of HCC, and DEN/CCl4-induced tumor models are not strongly consistent due to individual differences among mice and the sample sizes. Anyway, the above conclusions indicate good prognosis and may serve as a novel therapeutic target for HCC immunotherapy. Taken together, we determined the specific chemokines in either the tumor core region or IIE, which have remarkably different roles in clinical applications due to spatial heterogeneity in gene expression. Notably, the recruiting mechanism of these chemokines to immune cells still needs further exploration.

In conclusion, our study comprehensively reveals intratumor heterogeneity, especially immune-ITH, in HCC based on spatial transcriptomics technology. We further reveal the spatial expression patterns in specific regions of some key molecules such as CCL15, CCL19, and CCL21, which affect the infiltration and recruitment of various immune cells and collectively promote intratumor heterogeneity in the HCC microenvironment, thus influencing the prognosis of HCC patients. Our studies also highlight the clinical significance of the spatial heterogeneity and gene expression patterns, laying the foundation for developing new prognostic markers and therapeutic strategies for HCC.

## Abbreviations

AAV: adeno-associated virus; AUC: area under curves; DCs: dendritic cells; DEGs: differentially expressed genes; EMT: epithelial-mesenchymal transition; FFPE: formalin-fixed paraffin-embedded; HCC: hepatocellular carcinoma; HE: hematoxylin-eosin staining; IIE: immune infiltration enrichment; ISME: immunosuppressive microenvironment; ITH: intratumor heterogeneity; OCT: optimal cutting temperature; OS: overall survival; PLC: primary liver cancer; RFS: recurrence-free survival; ROC: receiver operating characteristic curve; sc-RNA seq: single cell RNA sequencing; ST: spatial transcriptomics; TAMs: tumor-associated macrophages; TME: tumor microenvironment; UMAP: uniform manifold approximation and projection; UMI: unique molecular identifier.

## Supplementary Material

Supplementary methods, figures and tables.
https://www.thno.org/v12p4163s1.pdf

## Acknowledgements

This research was supported by grants from the National Natural Science Foundation of China (nos. 81972657, 81830085 and 81972575); National Key Research and Development Program of China (2016YFC1302303); Shanghai Rising-Star Program (19QA1408700).

### Author Contributions

Study concept and design: Fu Yang; Acquisition of data: Yue-fan Wang, Sheng-xian Yuan, Hui Jiang, Zhi-xuan Li, Jian Tan, Zhi-hui Dai, Hao-zan Yin, Chun-mei Ge; Analysis and interpretation of data: Yue-fan Wang, Sheng-xian Yuan, Hui Jiang, Shu-han Sun and Fu Yang; Statistical analysis: Yue-fan Wang and Zhi-xuan Li; Drafting of the manuscript: Yue-fan Wang and Fu Yang; Critical revision of the manuscript: Fu Yang, Shu-han Sun, Sheng-xian Yuan and Hui Jiang; Obtained funding: Fu Yang, Shu-han Sun and Sheng-xian Yuan.

## Competing Interests

The authors have declared that no competing interest exists.

## References

1. Sung H, Ferlay J, Siegel RL, Laversanne M, Soerjomataram I, Jemal A, et al. Global Cancer Statistics 2020: GLOBOCAN Estimates of Incidence and Mortality Worldwide for 36 Cancers in 185 Countries. CA Cancer J Clin. 2021; 71: 209-49.

2. Romano L, Paladini S, Galli C, Raimondo G, Pollicino T, Zanetti AR. Hepatitis B vaccination. Hum Vaccin Immunother. 2015; 11: 53-7.
3. Ma L, Wang L, Khatib SA, Chang CW, Heinrich S, Dominguez DA, et al. Single-cell atlas of tumor cell evolution in response to therapy in hepatocellular carcinoma and intrahepatic cholangiocarcinoma. J Hepatol. 2021.
4. Nault JC, Villanueva A. Intratumor molecular and phenotypic diversity in hepatocellular carcinoma. Clin Cancer Res. 2015; 21: 1786-8.
5. Torrecilla S, Sia D, Harrington AN, Zhang Z, Cabellos L, Cornella H, et al. Trunk mutational events present minimal intra- and inter-tumoral heterogeneity in hepatocellular carcinoma. J Hepatol. 2017; 67: 1222-31.
6. Craig AJ, von Felden J, Garcia-Lezana T, Sarcognato S, Villanueva A. Tumour evolution in hepatocellular carcinoma. Nat Rev Gastroenterol Hepatol. 2020; 17: 139-52.
7. Nguyen PHD, Ma S, Phua CZJ, Kaya NA, Lai HLH, Lim CJ, et al. Author Correction: Intratumoural immune heterogeneity as a hallmark of tumour evolution and progression in hepatocellular carcinoma. Nat Commun. 2021; 12: 1372.
8. Ma L, Hernandez MO, Zhao Y, Mehta M, Tran B, Kelly M, et al. Tumor Cell Biodiversity Drives Microenvironmental Reprogramming in Liver Cancer. Cancer Cell. 2019; 36: 418-30 e6.
9. Losic B, Craig AJ, Villacorta-Martin C, Martins-Filho SN, Akers N, Chen X, et al. Intratumoral heterogeneity and clonal evolution in liver cancer. Nat Commun. 2020; 11: 291.
10. Kurebayashi Y, Ojima H, Tsujikawa H, Kubota N, Maehara J, Abe Y, et al. Landscape of immune microenvironment in hepatocellular carcinoma and its additional impact on histological and molecular classification. Hepatology. 2018; 68: 1025-41.
11. Zhang Q, He Y, Luo N, Patel SJ, Han Y, Gao R, et al. Landscape and Dynamics of Single Immune Cells in Hepatocellular Carcinoma. Cell. 2019; 179: 829-45 e20.
12. Zheng C, Zheng L, Yoo JK, Guo H, Zhang Y, Guo X, et al. Landscape of Infiltrating T Cells in Liver Cancer Revealed by Single-Cell Sequencing. Cell. 2017; 169: 1342-56 e16.
13. Yin Z, Dong C, Jiang K, Xu Z, Li R, Guo K, et al. Heterogeneity of cancer-associated fibroblasts and roles in the progression, prognosis, and therapy of hepatocellular carcinoma. J Hematol Oncol. 2019; 12: 101.
14. Ramachandran P, Matchett KP, Dobie R, Wilson-Kanamori JR, Henderson NC. Single-cell technologies in hepatology: new insights into liver biology and disease pathogenesis. Nat Rev Gastroenterol Hepatol. 2020; 17: 457-72.
15. Stahl PL, Salmen F, Vickovic S, Lundmark A, Navarro JF, Magnusson J, et al. Visualization and analysis of gene expression in tissue sections by spatial transcriptomics. Science. 2016; 353: 78-82.
16. Maniatis S, Aijo T, Vickovic S, Braine C, Kang K, Mollbrink A, et al. Spatiotemporal dynamics of molecular pathology in amyotrophic lateral sclerosis. Science. 2019; 364: 89-93.
17. Chen WT, Lu A, Craessaerts K, Pavie B, Sala Frigerio C, Corthout N, et al. Spatial Transcriptomics and *In situ* Sequencing to Study Alzheimer's Disease. Cell. 2020; 182: 976-91 e19.
18. Asp M, Giacomello S, Larsson L, Wu C, Furth D, Qian X, et al. A Spatiotemporal Organ-Wide Gene Expression and Cell Atlas of the Developing Human Heart. Cell. 2019; 179: 1647-60 e19.
19. Berglund E, Maaskola J, Schultz N, Friedrich S, Marklund M, Bergenstrahle J, et al. Spatial maps of prostate cancer transcriptomes reveal an unexplored landscape of heterogeneity. Nat Commun. 2018; 9: 2419.
20. Thrane K, Eriksson H, Maaskola J, Hansson J, Lundeberg J. Spatially Resolved Transcriptomics Enables Dissection of Genetic Heterogeneity in Stage III Cutaneous Malignant Melanoma. Cancer Res. 2018; 78: 5970-9.
21. Moncada R, Barkley D, Wagner F, Chiodin M, Devlin JC, Baron M, et al. Integrating microarray-based spatial transcriptomics and single-cell RNA-seq reveals tissue architecture in pancreatic ductal adenocarcinomas. Nat Biotechnol. 2020; 38: 333-42.
22. Zhao N, Zhang Y, Cheng R, Zhang D, Li F, Guo Y, et al. Spatial maps of hepatocellular carcinoma transcriptomes highlight an unexplored landscape of heterogeneity and a novel gene signature for survival. Cancer Cell Int. 2022; 22: 57.
23. Wu R, Guo W, Qiu X, Wang S, Sui C, Lian Q, et al. Comprehensive analysis of spatial architecture in primary liver cancer. Sci Adv. 2021; 7: eabg3750.
24. Vickovic S, Eraslan G, Salmen F, Klughammer J, Stenbeck L, Schapiro D, et al. High-definition spatial transcriptomics for *in situ* tissue profiling. Nat Methods. 2019; 16: 987-90.
25. Korsunsky I, Millard N, Fan J, Slowikowski K, Zhang F, Wei K, et al. Fast, sensitive and accurate integration of single-cell data with Harmony. Nat Methods. 2019; 16: 1289-96.
26. Zheng X, Liu X, Lei Y, Wang G, Liu M. Glypican-3: A Novel and Promising Target for the Treatment of Hepatocellular Carcinoma. Front Oncol. 2022; 12: 824208.
27. Ye X, Li C, Zu X, Lin M, Liu Q, Liu J, et al. A Large-Scale Multicenter Study Validates Aldo-Keto Reductase Family 1 Member B10 as a Prevalent Serum Marker for Detection of Hepatocellular Carcinoma. Hepatology. 2019; 69: 2489-501.
28. Liu T, Zhou L, Li D, Andl T, Zhang Y. Cancer-Associated Fibroblasts Build and Secure the Tumor Microenvironment. Front Cell Dev Biol. 2019; 7: 60.
29. Puck A, Kunig S, Modak M, May L, Fritz P, Battin C, et al. The soluble cytoplasmic tail of CD45 regulates T-cell activation via TLR4 signaling. Eur J Immunol. 2021; 51: 3176-85.
30. Tomescu C, Kroll K, Colon K, Papasavvas E, Frank I, Tebas P, et al. Identification of the predominant human NK cell effector subset mediating ADCC against HIV-infected targets coated with BNAbs or plasma from PLWH. Eur J Immunol. 2021; 51: 2051-61.
31. Vera-Lozada G, Segges P, Stefanoff CG, Barros MHM, Niedobitek G, Hassan R. Pathway-focused gene expression profiles and immunohistochemistry detection identify contrasting association of caspase 3 (CASP3) expression with prognosis in pediatric classical Hodgkin lymphoma. Hematol Oncol. 2018; 36: 663-70.
32. Zhao Y, Li ZX, Zhu YJ, Fu J, Zhao XF, Zhang YN, et al. Single-Cell Transcriptome Analysis Uncovers Intratumoral Heterogeneity and Underlying Mechanisms for Drug Resistance in Hepatobiliary Tumor Organoids. Adv Sci (Weinh). 2021; 8: e2003897.
33. Ng KT, Yeung OW, Lam YF, Liu J, Liu H, Pang L, et al. Glutathione S-transferase A2 promotes hepatocellular carcinoma recurrence after liver transplantation through modulating reactive oxygen species metabolism. Cell Death Discov. 2021; 7: 188.
34. Emma MR, Iovanna JL, Bachvarov D, Puleio R, Loria GR, Augello G, et al. NUPR1, a new target in liver cancer: implication in controlling cell growth, migration, invasion and sorafenib resistance. Cell Death Dis. 2016; 7: e2269.
35. Liu LZ, Zhang Z, Zheng BH, Shi Y, Duan M, Ma LJ, et al. CCL15 Recruits Suppressive Monocytes to Facilitate Immune Escape and Disease Progression in Hepatocellular Carcinoma. Hepatology. 2019; 69: 143-59.
36. Park ER, Kim SB, Lee JS, Kim YH, Lee DH, Cho EH, et al. The mitochondrial hinge protein, UQCRH, is a novel prognostic factor for hepatocellular carcinoma. Cancer Med. 2017; 6: 749-60.
37. Itatani Y, Kawada K, Fujishita T, Kakizaki F, Hirai H, Matsumoto T, et al. Loss of SMAD4 from colorectal cancer cells promotes CCL15 expression to recruit CCR1+ myeloid cells and facilitate liver metastasis. Gastroenterology. 2013; 145: 1064-75 e11.
38. Yamamoto T, Kawada K, Itatani Y, Inamoto S, Okamura R, Iwamoto M, et al. Loss of SMAD4 Promotes Lung Metastasis of Colorectal Cancer by Accumulation of CCR1+ Tumor-Associated Neutrophils through CCL15-CCR1 Axis. Clin Cancer Res. 2017; 23: 833-44.
39. Inamoto S, Itatani Y, Yamamoto T, Minamiguchi S, Hirai H, Iwamoto M, et al. Loss of SMAD4 Promotes Colorectal Cancer Progression by Accumulation of Myeloid-Derived Suppressor Cells through the CCL15-CCR1 Chemokine Axis. Clin Cancer Res. 2016; 22: 492-501.
40. Yang Q, Guo N, Zhou Y, Chen J, Wei Q, Han M. The role of tumor-associated macrophages (TAMs) in tumor progression and relevant advance in targeted therapy. Acta Pharm Sin B. 2020; 10: 2156-70.
41. Comerford I, Harata-Lee Y, Bunting MD, Gregor C, Kara EE, McColl SR. A myriad of functions and complex regulation of the CCR7/CCL19/CCL21 chemokine axis in the adaptive immune system. Cytokine Growth Factor Rev. 2013; 24: 269-83.
42. Forster R, Davalos-Misslitz AC, Rot A. CCR7 and its ligands: balancing immunity and tolerance. Nat Rev Immunol. 2008; 8: 362-71.
43. Pickens SR, Chamberlain ND, Volin MV, Pope RM, Mandelin AM, 2nd, Shahrara S. Characterization of CCL19 and CCL21 in rheumatoid arthritis. Arthritis Rheum. 2011; 63: 914-22.
44. Salem A, Alotaibi M, Mroueh R, Basheer HA, Afarinkia K. CCR7 as a therapeutic target in Cancer. Biochim Biophys Acta Rev Cancer. 2021; 1875: 188499.
45. de Chaisemartin L, Goc J, Damotte D, Validire P, Magdeleinat P, Alifano M, et al. Characterization of chemokines and adhesion molecules associated with T cell presence in tertiary lymphoid structures in human lung cancer. Cancer Res. 2011; 71: 6391-9.
46. Lin Y, Sharma S, John MS. CCL21 Cancer Immunotherapy. Cancers (Basel). 2014; 6: 1098-110.
47. Hong CY, Lee HJ, Kim HJ, Lee JJ. The lymphoid chemokine CCL21 enhances the cytotoxic T lymphocyte-inducing functions of dendritic cells. Scand J Immunol. 2014; 79: 173-80.
48. Wu ZH, Yang DL, Wang L, Liu J. Epigenetic and Immune-Cell Infiltration Changes in the Tumor Microenvironment in Hepatocellular Carcinoma. Front Immunol. 2021; 12: 793343.
49. Feng Y, Liu L, Li J, Huang J, Xie JH, Menard L, et al. Systematic characterization of the tumor microenvironment in Chinese patients with hepatocellular carcinoma highlights intratumoral B cells as a potential immunotherapy target. Oncol Rep. 2022; 47.
50. Liu F, Liu W, Sanin DE, Jia G, Tian M, Wang H, et al. Heterogeneity of exhausted T cells in the tumor microenvironment is linked to patient survival following resection in hepatocellular carcinoma. Oncoimmunology. 2020; 9: 1746573.
51. Lu LC, Hsu CH, Hsu C, Cheng AL. Tumor Heterogeneity in Hepatocellular Carcinoma: Facing the Challenges. Liver Cancer. 2016; 5: 128-38.
52. Ho DW, Tsui YM, Chan LK, Sze KM, Zhang X, Cheu JW, et al. Single-cell RNA sequencing shows the immunosuppressive landscape and tumor heterogeneity of HBV-associated hepatocellular carcinoma. Nat Commun. 2021; 12: 3684.
53. Dong X, Wang F, Liu C, Ling J, Jia X, Shen F, et al. Single-cell analysis reveals the intra-tumor heterogeneity and identifies MLXIPL as a biomarker in the cellular trajectory of hepatocellular carcinoma. Cell Death Discov. 2021; 7: 14.

54. Ospina OE, Wilson CM, Soupir AC, Berglund A, Smalley I, Tsai KY, et al. spatialGE: Quantification and visualization of the tumor microenvironment heterogeneity using spatial transcriptomics. Bioinformatics. 2022.
55. Nguyen PHD, Ma S, Phua CZJ, Kaya NA, Lai HLH, Lim CJ, et al. Intratumoural immune heterogeneity as a hallmark of tumour evolution and progression in hepatocellular carcinoma. Nat Commun. 2021; 12: 227.
56. Wang C, Ma C, Gong L, Guo Y, Fu K, Zhang Y, et al. Macrophage Polarization and its Role in Liver Disease. Front Immunol. 2021; 12: 803037.